Ocean Dynamics (2012) 62:1073–1089
DOI 10.1007/s10236-012-0546-4

Backtracking drifting objects using surface currents from high-frequency (HF) radar technology

Ana Julia Abascal · Sonia Castanedo · Vicente Fernández · Raúl Medina

Received: 22 August 2011 / Accepted: 11 April 2012 / Published online: 12 May 2012

Abstract In this work, the benefits of high-frequency (HF) radar ocean observation technology for backtracking drifting objects are analysed. The HF radar performance is evaluated by comparison of trajectories between drifter buoys versus numerical simulations using a Lagrangian trajectory model. High-resolution currents measured by a coastal HF radar network combined with atmospheric fields provided by numerical models are used to backtrack the trajectory of two dataset of surface-drifting buoys: group I (with drogue) and group II (without drogue). A methodology based on optimization methods is applied to estimate the uncertainty in the trajectory simulations and to optimize the search area of the backtracked positions. The results show that, to backtrack the trajectory of the buoys in group II, both currents and wind fields were required. However, wind fields could be practically discarded when simulating the trajectories of group I. In this case, the optimal backtracked trajectories were obtained using only HF radar currents as forcing. Based on the radar availability data, two periods ranging between 8 and 10 h were selected to backtrack the buoy trajectories. The root mean squared error (RMSE) was found to be 1.01 km for group I and 0.82 km for group II. Taking into account these values, a search area was calculated using circles of RMSE radii, obtaining 3.2 and 2.11 km^2 for groups I and II, respectively. These results show the positive contribution of HF radar currents for backtracking drifting objects and demonstrate that these data combined with atmospheric models are of value to perform backtracking analysis of drifting objects.

Keywords HF radar currents · Backtracking · Drifting buoys · Lagrangian trajectory model · Search and rescue (SAR)

Responsible Editor: Oyvind Breivik

This article is part of the Topical Collection on *Advances in Search and Rescue at Sea*

A. J. Abascal (✉) · S. Castanedo · R. Medina
Environmental Hydraulics Institute "IH Cantabria",
Universidad de Cantabria,
C/Isabel Torres no. 15,
39011 Santander, Spain
e-mail: abascalaj@unican.es

V. Fernández
Qualitas Remos,
C/Toronga, 31,
28043 Madrid, Spain

1 Introduction

The recent development of high-frequency (HF) coastal radar technology has motivated its use for many oceanographic practical applications, such as oil spill response and maritime search and rescue (SAR) operations (e.g. Hodgins 1991; Ullman et al. 2003; O'Donnell et al. 2005). One of these activities is the estimation of the origin of an object in the sea, a complex process that could be improved by the use of data obtained from this new ocean observing technology. Backtracking drifting objects trajectories is of great importance for a number of marine operations. For example, in oil spill response preparedness, the simulation back in time of an oil slick could be crucial for detecting likely release sites and illegal discharges and to identify potential polluters. For marine safety and SAR activities, this back drift estimation technique could be useful for multiple purposes, for instance, to locate the origin of a debris field, to identify the origin of uncontrolled drift floating objects, to locate the origin of a marine accident if a shipwreck appears

in the sea or even in the search of the wreckage area in the case of an aircraft accident.

During the last years, Lagrangian trajectory models based on hydrodynamic and atmospheric models have been widely used to predict the trajectory of floating objects, mainly for oil spill response (e.g. Spaulding et al. 1992; Miranda et al. 2000; Beegle-Krause 2001; Daniel et al. 2003; Castanedo et al. 2006). For SAR activities, several operational forecast models have been developed recently to predict the evolution of search and rescue objects and objects containing hazardous material (Hackett et al. 2006; Breivik and Allen 2008; Davidson et al. 2009). Besides forecast applications, Lagrangian trajectory models have been recently used and incorporated in operational systems for backtracking purposes (Ambjörn 2008; Christiansen 2003). The challenge of backtracking is to simulate back in time the path followed by a floating object given its final location and the evolution of the atmospheric and oceanographic fields. However, the estimation of the origin of drifting objects is a difficult task due to the uncertainties in drift properties and environmental conditions. The success of the simulation depends on the formulation of the Lagrangian model itself and also on the accuracy of the forcing data (wind, waves and currents), usually provided by numerical models (Sebastiao and Soares 2006). These atmospheric and oceanographic models have their own intrinsic errors, which may affect the accuracy of the simulations (Edwards et al. 2006; Price et al. 2006). The uncertainty in the forcing becomes more important in coastal areas, where the complex pattern that characterizes the slope currents and the high mesoscale activity complicate an accurate forecasting of the current field. Moreover, even small errors in the estimation of ocean currents can drastically change particle trajectories (Griffa et al. 2004).

In order to address this problem, HF coastal radar observation systems have become an alternative to provide accurate current surface maps in real time in near-coastal environments. HF radar surface currents have been validated with many different types of in situ current measurements, including surface drifters and subsurface current meters (e.g. Kohut et al. 2006). A general review of the validation studies can be found in Chapman et al. (1997) and Chapman and Graber (1997). These works show that the remote sensing of surface currents in coastal areas using HF radar systems is an accurate technology (Chapman et al. 1997), being therefore suitable for oceanographic practical applications as forcing for Lagrangian trajectory models in an emergency response at sea (Abascal et al. 2009b).

Due to the new potential capabilities offered by this observation technology, several studies have been carried out to assess the effectiveness of trajectory analysis using currents derived from HF radar (Ullman et al. 2003, 2006; O'Donnell et al. 2005; Abascal et al. 2009b). In order to use this technology for forecasting, some authors have developed forecasting algorithms to use HF radar data to make short-term surface current predictions (O'Donnell et al. 2005; Barrick et al., manuscript submitted for publication). However, HF radar systems provide actual measurements of surface currents and, consequently, it presents a great potential for backtracking purposes.

In this work, the benefits of HF radar currents for backtracking drifting objects are analysed. To achieve this objective, high-resolution currents measured by a coastal HF radar network are used together with a Lagrangian trajectory model for backtracking purposes. HF radar currents combined with atmospheric fields provided by numerical models are used with a Lagrangian trajectory model to backtrack the trajectory of two datasets of different drifting buoys collected during an exercise of the DRIFTER project (ERA-net AMPERA, VI European Framework Programme). In order to provide accurate results, a methodology based on optimization methods is applied to estimate the uncertainty in the trajectory simulations and to define the probability density distribution of the backtracked positions. In this methodology, the transport model is calibrated by means of a global optimization algorithm in order to obtain the optimal model parameters and their corresponding 95 % confidence interval for each buoys dataset. Subsequently, the calibration results are used to compute the buoy trajectories using Monte Carlo approach. Finally, the 95 % confidence areas are determined by means of a bivariate kernel estimator. The accuracy of the backtracked trajectories is evaluated by comparison of actual buoy trajectories with the simulations performed. It is worth to mention that the present study represents one of the first attempts to analyse the benefit of using HF radar technology for backtracking purposes on the Spanish coast.

The remainder of this article is organized as follows: "Section 2" presents a review of the data used for this study, "Section 3" describes the methodology used for the backtracking, "Section 4" presents the results and "Section 5" summarizes the main conclusions of the study.

2 Data

The drifter data used in this work was collected during an exercise developed within the framework of the project DRIFTER: "HNS, oil and inert pollution: Trajectory modelling and monitoring" (AMPERA, ERA-net VI European Framework Programme). One of the issues of this project was the testing and application of drifting buoys to follow oil spills (Allen-Perkins et al. 2010). As part of the project, several sets of experiments were carried out by INTECMAR (Instituto Tecnológico para el Control del Medio Marino de Galicia) in order to study the influence of ocean–meteorological conditions and buoy features on the drifting trajectory (http://www.intecmar.org/drifter/).

During one of these aforementioned exercises (further referred to as DRIFTER Exercise), a set of 13 buoys was released in the Bay of Vigo (Galicia, Spain) between September 14, 2010 and September 15, 2010 (Allen-Perkins et al. 2010). To study the influence of the buoy features on the drifting trajectory, two datasets of drifting buoys were used. Moreover, an operational system was established to simulate the trajectories of the buoys. As part of this operational system, surface currents from radar HF and wind provided by numerical models were available in real time and were used to simulate the trajectory of the buoys (Fernández et al. 2010).

After the operational exercise, all the ocean and meteorological data collected during the exercise were used to simulate the buoy trajectories and more specifically to study the benefits of using radar currents for backtracking purposes. A description of this database is provided in this section.

2.1 Buoy data

As mentioned previously, in order to study the influence of buoy features on drifting trajectory, two datasets of drifting buoys were used in the DRIFTER exercise. The buoys in the first group (model MD02, http://www.albatrosmt.com/) consist of a cylinder 25 cm in height and 10 cm in diameter with a 60-cm flexible drogue (see Fig. 1a). The transmission of the buoy location was performed via GSM modem technology. On the other hand, the second group was made up of six small buoys of 31 cm in height and 45 cm in diameter without drogue (model MLi, http://www.marineinstruments.es/) (see Fig. 1b). In this case, the transmission was done by satellite through the Iridium network. All the buoys provided a 15-min sampling rate of their positions. Unfortunately, some of the buoys ceased to emit some hours after their deployment and were discarded for the present study.

For the sake of clarity, MD02 and MLi buoys have been included in two different groups, hereinafter called group I and group II, respectively. A summary of the buoy dataset used in this study is presented in Table 1, including drifter model, group, name of the institution in charge of the buoy deployment, date of the first and final record and temporal resolution of the data.

Figure 2 shows the study area, the Bay of Vigo in northwestern Spain, and the path followed by the buoys during the study period, which spans from September 14 10:30 UTC to September 15 (see Table 1). The buoys deployment is indicated by a black circle. As can be seen in Fig. 2, the drifters moved towards the west and south during September 14 and reversed their direction and started to move towards the northeast on September 15, drifting into the Bay of Vigo. The path followed by the buoys shows the great variability in the transport of drifting objects. Although all the buoys were released at the same place and time, they followed different trajectories and present a different final position.

2.2 HF radar currents

A HF radar system is a land-based technology capable of measuring ocean surface currents from the backscattered radar signal given by ocean surface gravity waves (Barrick et al. 1977). HF radar system works on the principle of Bragg scattering where the transmitted electromagnetic radio waves were reflected by resonant ocean surface waves of one half the incident radar wavelength. A HF radar system consists of a transmitter antenna capable of transmitting high-frequency (3–50 MHz) electromagnetic waves over a conductive ocean surface and receiver antennas capable of capturing the signal backscattered and with a Doppler frequency shift by moving ocean surface due to waves and underlying (surface) currents.

HF radar surface currents employed in this study were provided by the high-resolution HF radar network at the Bay of Vigo owned and operated by University of Vigo (Varela 2010). The HF radar network consists of two CODAR systems, one located at Punta Subrido (SUBR) in the northern entrance of the Bay and the other at Isla de Toralla

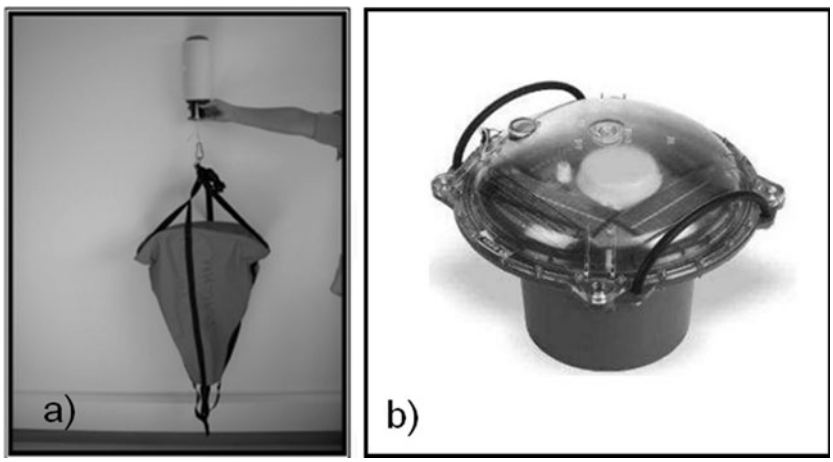

Fig. 1 MD02 (**a**) and MLi (**b**) drifting buoys (taken from Allen-Perkins et al. (2010))

Table 1 Buoys deployed during the "DRIFTER Exercise". The periods of the simulated trajectories are also shown

Drifter model	Group	Buoy's number (ID)	Institution	Buoys trajectories		Δt (min)	Periods of simulation			
							Period 1		Period 2	
				Initial date (UTC)	Final date (UTC)		Initial date (UCT)	Final date (UTC)	Initial date (UCT)	Final date (UTC)
MD02	I	1	INTECMAR	09/14/2010 10:30	09/15/2010 17:00	15	09/14/2010 10:30	09/14/2010 22:00	09/15/2010 08:30	09/15/2010 17:00
MD02	I	2	INTECMAR	09/14/2010 10:30	09/15/2010 10:00	15	09/14/2010 10:30	09/14/2010 22:00		
MD02	I	3	INTECMAR	09/14/2010 10:30	09/15/2010 17:00	15	09/14/2010 10:30	09/14/2010 22:00	09/15/2010 08:30	09/15/2010 17:00
MD02	I	4	INTECMAR	09/14/2010 10:30	09/15/2010 15:00	15	09/14/2010 10:30	09/14/2010 22:00	09/15/2010 08:30	09/15/2010 15:00
MLi	II	5	INTECMAR	09/14/2010 10:30	09/15/2010 17:00	15	09/14/2010 10:30	09/14/2010 22:00	09/15/2010 08:30	09/15/2010 14:00
MLi	II	6	INTECMAR	09/14/2010 10:30	09/15/2010 17:00	15	09/14/2010 10:30	09/14/2010 22:00	09/15/2010 08:30	09/15/2010 14:00
MLi	II	7	INTECMAR	09/14/2010 10:30	09/15/2010 17:00	15	09/14/2010 10:30	09/14/2010 22:00	09/15/2010 08:30	09/15/2010 14:00
MLi	II	8	INTECMAR	09/14/2010 10:30	09/15/2010 17:00	15	09/14/2010 10:30	09/14/2010 22:00	09/15/2010 08:30	09/15/2010 13:00
MLi	II	9	INTECMAR	09/14/2010 10:30	09/15/2010 17:00	15	09/14/2010 10:30	09/14/2010 22:00	09/15/2010 08:30	09/15/2010 12:00

(TORA) in the southern part of the Bay (Fig. 3). The TORA system operates at a central frequency of 46.2 MHz with a bandwidth of 400 kHz and a sweep rate of 4 Hz, while SUBR system operates at a central frequency of 46.8 MHz with a bandwidth of 400 kHz and a sweep rate of 4 Hz. With these specifications, each radar system measures radial components of the surface current with an average range of 15 km and a range resolution of 375 m. The radial vector files generated by the two CODAR systems at 30-min intervals were combined with respect to a predefined surface grid of 0.4×0.4-km horizontal resolution using the method of least squares (Lipa and Barrick 1983) to generate the total vector field. A typical total vector plot for this system is shown in Fig. 3. It is important to note here that, due to the technical characteristics of the radar system, the effective depth is of the order of 0.25 m (Stewart and Joy 1974).

During the radar exercise period, the HF network has been running operationally and providing surface current

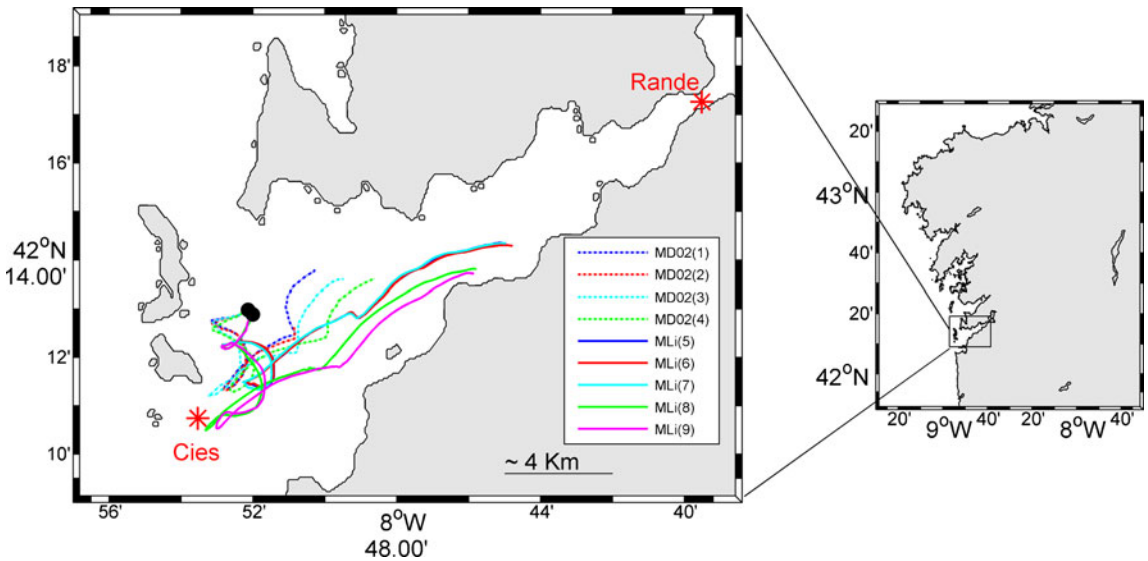

Fig. 2 Study area and buoy trajectories. The *black circle* represents the buoys deployment. *Dashed* and *solid lines* represent the MD02 (with drogue) and MLi (without drogue) buoys. The buoy trajectories span from September 14 10:30 UTC to September 15 (see Table 1 for more details). Locations of the ocean–meteorological stations (*red asterisks*) used for atmospheric validation are also shown

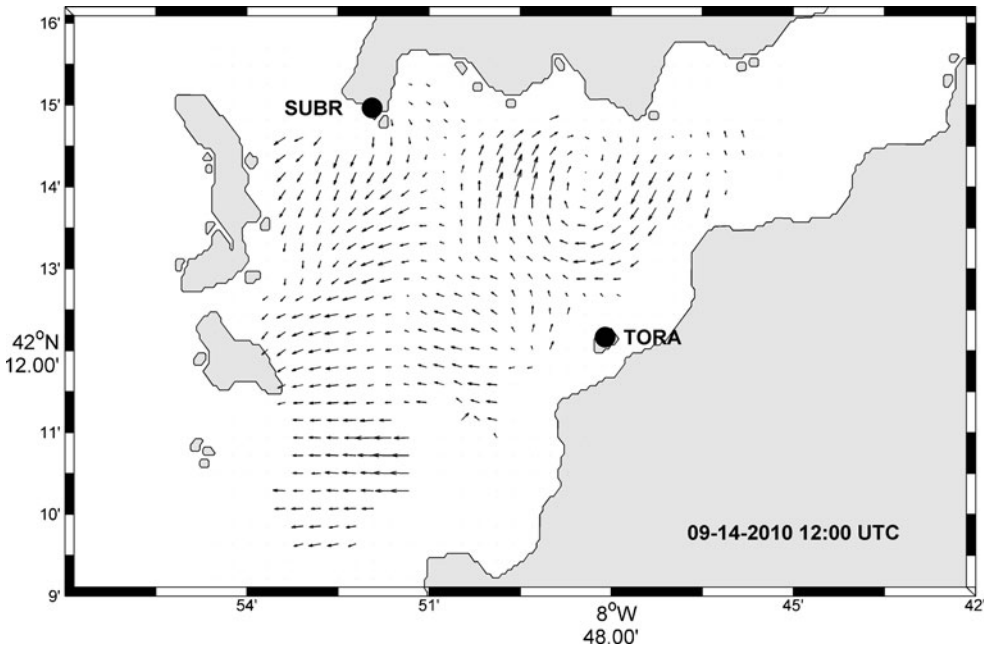

Fig. 3 Typical surface current map provided by the high-resolution Bay of Vigo coastal HF radar system of the University of Vigo. The radar site locations are indicated by *solid black circles*

data in real time. There was, however, a problem with the power supply of the SUBR system which led to a gap in the total surface currents for the period between September 14, 2010 22:30 and September 15, 2010 08:00 UTC.

2.3 Atmospheric data

The atmospheric forcing fields were provided by the operational systems of the regional meteorological agency in Galicia (MeteoGalicia). The wind fields are the output of the WRF model (Weather Research and Forecasting) (Skamarock et al. 2005). The data consist of 10 m wind speed and direction, provided with a 4-km spatial resolution and with a 1-h time interval.

Operational models running in MeteoGalicia are validated using data provided by the network of ocean variables in the Galician coast (Balseiro 2008). Figure 2 shows the location of two met-ocean stations in the Ria de Vigo (indicated by red asterisks). One of these stations is located in the strait of Rande and the other one is mounted on an oceanic buoy, located south of the Cies Islands. These stations, which collect meteorological data, such as temperature, humidity and wind, were deployed and used to carry out the atmospheric validation during EASY project (Balseiro 2008).

3 Methodology

A Lagrangian trajectory model forced with HF radar currents and wind numerical data was used to backtrack the trajectories of drifting buoys and to study the benefits of using HF current fields for backtracking analysis. The uncertainty in the trajectory simulations was calculated following the methodology proposed by Abascal et al. (2009b). Based on this methodology, model parameters and uncertainty were estimated by means of optimization methods and used to calculate the probable distribution of the backtracked trajectories.

For each dataset of drifting buoys, the Lagrangian trajectory model was calibrated to minimize the global differences regarding the actual buoy trajectories. As a result of the calibration process, the optimum mean value and the corresponding 95 % confidence interval for each model parameter was obtained. Once calibrated, the model was used to perform the final simulations. This procedure has the following two advantages: (a) the calibration process includes the sources of uncertainty into the model calibration coefficients, providing the optimal backtracked trajectory and (b) the values of the coefficients provide additional information regarding the relevance of each forcing (wind and currents) in the trajectory simulation.

Each backtracked trajectory was computed by means of a Monte Carlo approach using the results obtained in the calibration process. The 95 % confidence areas were determined and used to calculate the distance between the actual and numerical trajectories. The accuracy of the simulations was evaluated by comparison with actual buoy trajectories and quantified by means of key statistical parameters.

In this section, the Lagrangian trajectory model and the calibration methodology are described.

3.1 Lagrangian trajectory model

The model used in this work is the operational oil spill model called TESEO (Abascal et al. 2007). The numerical model consists of a transport and a weathering module to

represent the evolution of oil spilled in the marine environment. This work focuses on the use of the transport module to analyse the motion of the drifters deployed in the DRIFTER Exercise. The transport application derives from the two-dimensional Lagrangian transport model PICHI, developed by the University of Cantabria as part of the operational forecasting system created in response to the *Prestige* oil spill (Castanedo et al. 2006). The drift process of the spilled oil is described by tracking a cloud of numerical particles equivalent to the oil slicks. The position of the particles is computed by the superposition of the transport induced by currents, wind and turbulent dispersion. The numerical model solves by means of the Euler method the following vector equation:

$$\frac{d\vec{x}}{dt} = \vec{u}_{\mathrm{a}}\left(\vec{x}_i, t\right) + \vec{u}_{\mathrm{d}}\left(\vec{x}_i, t\right) \tag{1}$$

where $\vec{x}_i$ is the particle position and $\vec{u}_a$ and $\vec{u}_d$ are the advective and diffusive velocities, respectively, in $\vec{x}_i$. The advective velocity, $\vec{u}_a$, is calculated as the linear combination of currents and wind velocity expressed as:

$$\vec{u}_{\mathrm{a}} = C_{\mathrm{C}}\,\vec{u}_{\mathrm{c}} + C_{\mathrm{D}}\,\vec{u}_{\mathrm{w}} \tag{2}$$

where $\vec{u}_{\mathrm{c}}$ is the surface current velocity, $\vec{u}_{\mathrm{w}}$ is the wind velocity at a height of 10 m over the sea surface and C_{D} is the wind drag coefficient.

Note that Eq. (2) includes a coefficient in the current term C_{C}. Usually in Lagrangian models, the current term is not affected by any coefficient. However, to take into account the uncertainty in the radar measurements, it was decided to include this coefficient to minimize the differences between actual and numerical trajectories.

The turbulent diffusive velocity is obtained using Monte Carlo sampling in the range of velocities $\left[-\vec{u}_{\mathrm{d}}, \vec{u}_{\mathrm{d}}\right]$ that are assumed proportional to the diffusion coefficients (Maier-Reimer 1982; Hunter et al. 1993). The velocity fluctuation for each time step, Δt, is defined as:

$$\left|\vec{u_{\mathrm{d}}}\right| = \sqrt{\frac{6D}{\Delta t}} \tag{3}$$

where D is the diffusion coefficient, typically in the range of 1–100 m^2/s (ASCE 1996).

Backtracking simulation is done by considering forcing data in reverse time and direction. Instead of going forward, the particles move backwards. By means of the backtracking, the model is able to simulate oil spills and drifting objects back in time, with the purpose of detecting the origin of the object.

The Lagrangian transport model has been calibrated and validated using data from drifting buoys (Abascal et al. 2007, 2009a). Moreover, it has been successfully tested during several operational oil spill exercises organized by the Spanish Maritime Safety and Rescue Agency (SASEMAR) with the collaboration of the ESEOO group (Abascal et al. 2007; Sotillo et al. 2008).

3.2 Transport model calibration

To apply Eq. (1), the model coefficients, C_{D} and C_{C}, have to be determined. The value of the wind drag coefficient, C_{D}, varies from 2.5 to 4.4 % of the wind speed, with a mean value of 3–3.5 % (ASCE 1996). Reed et al. (1994) suggests that, in light winds without breaking waves, 3.5 % of the wind speed in the direction of the wind provides a good simulation of the oil slick drift in offshore areas. Although it is possible to use coefficients that range between those reported in the literature, the work presented in Abascal et al. (2009a) shows the importance of obtaining the best-agreement model coefficients for the region of interest.

Therefore, the model calibration aims to find the optimal values of the model coefficients so as to minimize the global differences between numerical and actual trajectories provided by drifter observations.

In this study, the optimal coefficients of the model were obtained by means of the global optimization algorithm Shuffled Complex Evolution Metropolis (SCEM-UA) developed by the University of Arizona and the University of Amsterdam (Vrugt et al. 2003a, b). The SCEM-UA method is a general-purpose global optimization algorithm designed to infer the probability density function of the model parameters within a single optimization run (Vrugt et al. 2003a, b). This algorithm is a modified version of the original SCE-UA global optimization algorithm developed by Duan et al. (1992). The goal of the original SCE-UA algorithm is to find a single best parameter set in the feasible space. However, the SCEM-UA is able to infer both the most likely parameter set and its underlying posterior probability distribution. The SCEM-UA algorithm operates by merging the strengths of the Metropolis algorithm, controlled random search, competitive evolution and complex shuffling in order to continuously update the proposal distribution and evolve the sampler to the posterior target distribution (Vrugt et al. 2003a, b).

Following this methodology, the calibration of the transport model was formulated as an optimization problem, where an objective function, J, has to be minimized. In this case, the objective function was defined as:

$$J(\theta) = \sum_{j=1}^{T} \left[\begin{array}{l} \left(U_{\mathrm{B}x}\left(\vec{x}, t\right) - U_{\mathrm{M}x}\left(\vec{x}, t; \theta\right)\right)^2 \\ \quad + \left(U_{\mathrm{B}y}\left(\vec{x}, t\right) - U_{\mathrm{M}y}\left(\vec{x}, t; \theta\right)\right)^2 \end{array} \right] \tag{4}$$

Equation (4) represents the difference between the predicted trajectory and the buoy path. $U_{\mathrm{B}x}$ and $U_{\mathrm{B}y}$ are the buoy velocity components in the x (W–E) and y (N–S)

direction, respectively; U_{Mx} and U_{My} are the model velocity components in the x and y direction, respectively; $\overrightarrow{x}$ is the location of the buoys; T is the time period with buoy data; and $\theta = (C_D, C_C)$ is the vector of parameters to be obtained.

Previous tests were performed including D in the calibration process as a parameter of θ. However, the best results were obtained without this coefficient. This is due to the fact that the random behaviour of the diffusive velocity is included in the confidence intervals of the advective model parameters (C_D and C_C).

The buoy velocity, $\overrightarrow{U}_B$, was obtained from the tracked satellite positions, which have a temporal resolution of 15 min. The advective model velocity, $\overrightarrow{U}_M$, was calculated using Eq. (2) by means of the numerical data provided by the atmospheric model (wind data) and the radar currents collected during the exercise.

The SCEM-UA algorithm provides N combinations of model parameters $\{\theta_i = (C_{Di}, C_{Ci}), i = 1...N\}$ that minimize the function $J(\theta)$. For each model parameter, the N values obtained in the calibration process were used to calculate the corresponding histogram and the cumulative distribution function. Based on this statistical information, the mean values $\widehat{\theta} = \left(\widehat{C}_D, \widehat{C}_C\right)$ and the confidence interval at 95 % confidence level were estimated.

It is important to highlight that the calibration not only takes into account the physical processes but also includes the sources of uncertainty into the model calibration coefficients in order to provide the optimal simulated trajectories.

3.3 Estimation of confidence intervals for backtracked trajectories

To evaluate the curve that limits the 95 % confidence area of simulated trajectories, a bivariate kernel estimator (Martinez and Martinez 2002) was applied to calculate the two-dimensional density distribution for the N simulated positions. For a sample of size n, where each observation is a d-dimensional vector, X_i, i=1, …, n, the kernel density estimate is defined as (Martinez and Martinez 2002):

$$f_{Ker}(X) = \frac{1}{nh_1 \ldots h_d} \sum_{i=1}^{n} \left\{ \prod_{j=1}^{d} K\left(\frac{x_j - X_{ij}}{h_j}\right) \right\} \quad (5)$$

where X_{ij} is the j-th component of the i-th observation, K is the kernel function and h is the smoothing parameter or window width. The parameter h is defined as:

$$h_{j_{Ker}} = \left(\frac{4}{n(d+2)}\right)^{\frac{1}{d+4}} \sigma_j;\ \mathrm{j} = 1, \ldots, d, \quad (6)$$

where σ_j is the standard deviation of the j-th component.

The kernel equation for density estimation was considered as a Gaussian function:

$$K(x) = \frac{1}{\sqrt{2\pi}} \exp\left(\frac{-x^2}{2}\right) \quad (7)$$

4 Results

4.1 Calibration results

As mentioned previously, the transport model calibration was performed to obtain the optimal $\left(\widehat{C}_D, \widehat{C}_C\right)$ combination of coefficients for the two buoy datasets. Given the lack of HF current data from 09/14/2010 22:30 to 09/15/2010 08:00 UTC, the calibration focused on the larger period with continuous data (09/14/2010 10:30 UTC–09/14/2010 22:00 UTC).

The empirical probability density function of the model parameters obtained for groups I and II is presented in Fig. 4. The 95 % confidence interval limits are also shown.

With a 95 % confidence level, the wind drag coefficient minimizing Eq. (4) was found to be $\widehat{C}_D = 0.0004$ included in the interval (0, 0.0013) for group I. This value close to 0 shows that, for buoys in group I (buoys with 60-cm drogue), the contribution of atmospheric fields to the simulation of the buoy trajectories is practically negligible. In this case, the effect of the wind data could practically be discarded. These results could be influenced by the wind conditions during this period. On September 14, wind velocity was approximately 1.8 m/s. These calm wind conditions could contribute to reduce the direct effect of wind forcing on the buoy trajectories.

Regarding group II (buoys without drogue), with 95 % confidence level, the wind drag coefficient minimizing Eq. (4) was found to be $\widehat{C}_D = 0.015$ included in the interval (0.008, 0.022). This value is smaller than the most common value (3 % of the wind speed) used in Lagrangian trajectory models. This result is consistent with previous studies (Abascal et al. 2009b) and suggests that C_D accounts only for the wind-driven component resulting from the direct wind stress (sailing effect), whereas the HF radar currents contain the wind-induced component of the ocean surface current.

The comparison of the results obtained for groups I and II shows that wind forcing presents a higher relevance in the motion of the buoys belonging to Group II. This is not surprising given the features of this type of buoys (surface buoys without drogue). However, it shows the importance of properly determining the relative importance of each forcing in the transport and the appropriate coefficients in order to optimize the model results.

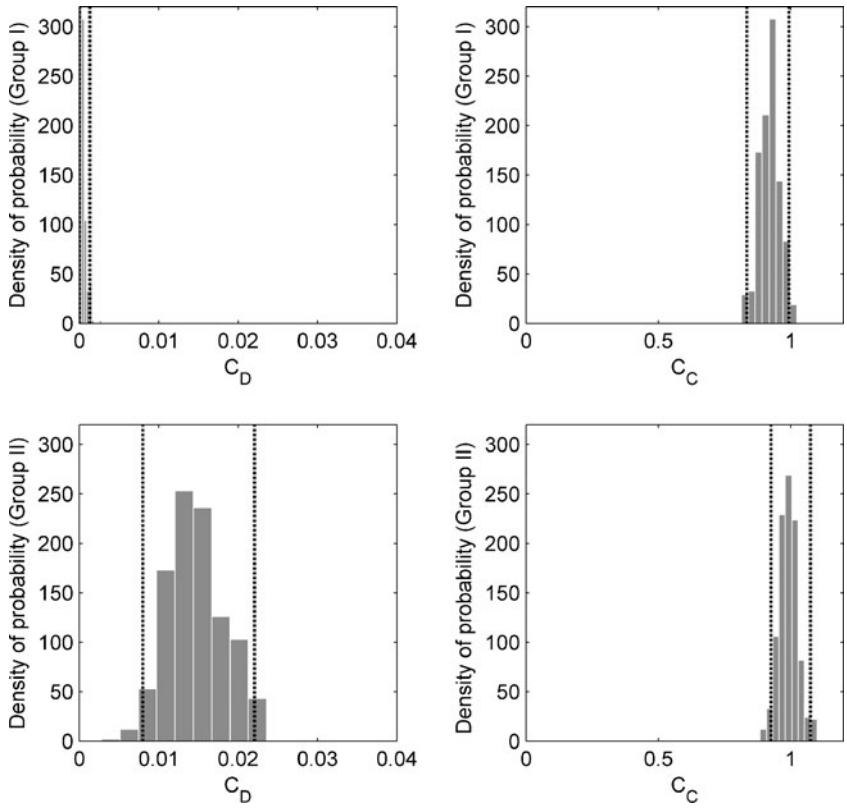

Fig. 4 Empirical probability density function for group I (*upper*) and group II (*lower*) obtained in the calibration process. C_D and C_C are shown in the *left* and *right panels*, respectively. The 95 % confidence interval limits are represented by the *dashed line*

Regarding the current coefficient results for groups I and II, the optimal current coefficient was found to be $\widehat{C}_C = 0.919$ included in the interval (0.835, 0.994) and $\widehat{C}_C = 0.990$ included in the interval (0.926, 1.075). Since $\widehat{C}_C$ represents the effect of the current on a trajectory of a floating drifter, a value close to 1, such as the one obtained with the radar, is desired. In contrast, using currents from global circulation models, Abascal et al. (2009a) found a value as low as $\widehat{C}_C = 0.266$, suggesting discrepancies between the real and numerical current fields. Sotillo et al. (2008), using currents from higher-resolution nested regional circulation models, obtained $\widehat{C}_C = 0.52$. These results show that the C_C value improves when using current data provided by regional circulation models. However, discrepancies between the real and numerical current fields are still present. In a later study, using currents measured by a long-range HF radar network, Abascal et al. (2009b) found a value of $\widehat{C}_C = 0.787$ showing the improvement of using observed HF currents radar instead of numerical model data. As shown above, this result is improved on this work using high-resolution coastal radar systems. The high C_C value obtained in the present study (close to 1) indicates a good agreement between the real current field and the radar HF current measurements and shows the improvement of using high-resolution observed HF currents radar. A summary of the aforementioned studies, including the data used and the results obtained, is presented in Table 2.

4.2 Trajectory analysis

The previously described TESEO transport model was used to backtrack the trajectories of the buoys. Based on the radar availability data, two different periods were considered (see Fig. 5):

1. From 09/14/2010 10:30 UTC to 09/14/2010 22:00 UTC, hereinafter called period 1. Note that this period was used for the calibration of the model.

Table 2 A summary of previous studies related to the calibration of the transport model

References	Buoy model	HF Radar data	Oceanographic models	Atmospheric model	Study region	$\widehat{C}_C$
Abascal et al. (2009a)	SC40 PTR	NO	NRLPOM MERCATOR	HIRLAM	Gulf of Biscay	0.266
Sotillo et al. (2008)	SC40 PTR	NO	ESEOAT	HIRLAM	Gulf of Biscay	0.520
Abascal et al. (2009b)	PTR	YES	NO	HIRLAM	Galician coast	0.787

2. From 09/15/2010 08:30 UTC to the final position of each buoy (see Table 1), hereinafter called period 2. Note that this period represents a dataset which is independent of the calibration process.

The final time of the simulations in period 2 was selected taking into account the end time of the buoy trajectories and the coverage area of the radar (see Table 1 and Fig. 3). The starting and end time for each buoy and period are shown in Table 1. Note that the trajectory of buoy number 2 has been discarded of the second period because of the short availability data (this buoy ended at 10:00 UTC).

Simulations were carried out for all the buoys in groups I and II starting at the final point of the selected periods (see Fig. 5). For each buoy, the backtracked trajectory was simulated using Monte Carlo approach based on the calibration results. The SCEM-UA algorithm provided N (N=1,000) optimal sets of parameters calculated by means of Markov Chain Monte Carlo process. To include this information in the trajectory analysis, a high number of simulations (N) were performed considering the N set of optimal model parameters $\{(C_{Di}, C_{Ci}) \ldots (C_{DN}, C_{CN})\}$. Each simulated trajectory was calculated as the mass centre of a cloud of 1,000 independent numerical particles. Simulations were performed using a 60-s time step. Taking into account the natural dispersion of the buoy trajectories, the diffusion coefficient was considered to be 2 m^2/s, a value included in the interval reported in the literature (ASCE 1996). The final position of the N simulated trajectories was different as a function of the combination of parameters used in the transport model (see Eq. (2)), providing an ensemble of numerical positions that define an area that represents the possible origin of the initial buoy trajectories.

A comparison between the actual and simulated backward trajectories for group I is shown in Fig. 6 (period 1) and Fig. 7 (period 2). Regarding group II, the results are shown in Fig. 8 (period 1) and Fig. 9 (period 2). In each panel of Figs. 6, 7, 8 and 9, the black line shows the actual buoy trajectory and the grey lines are the 1,000 simulated backward trajectories for the study period. The black dots show the numerical positions at the end of the simulation. Note that some of the backtracked trajectories shown in

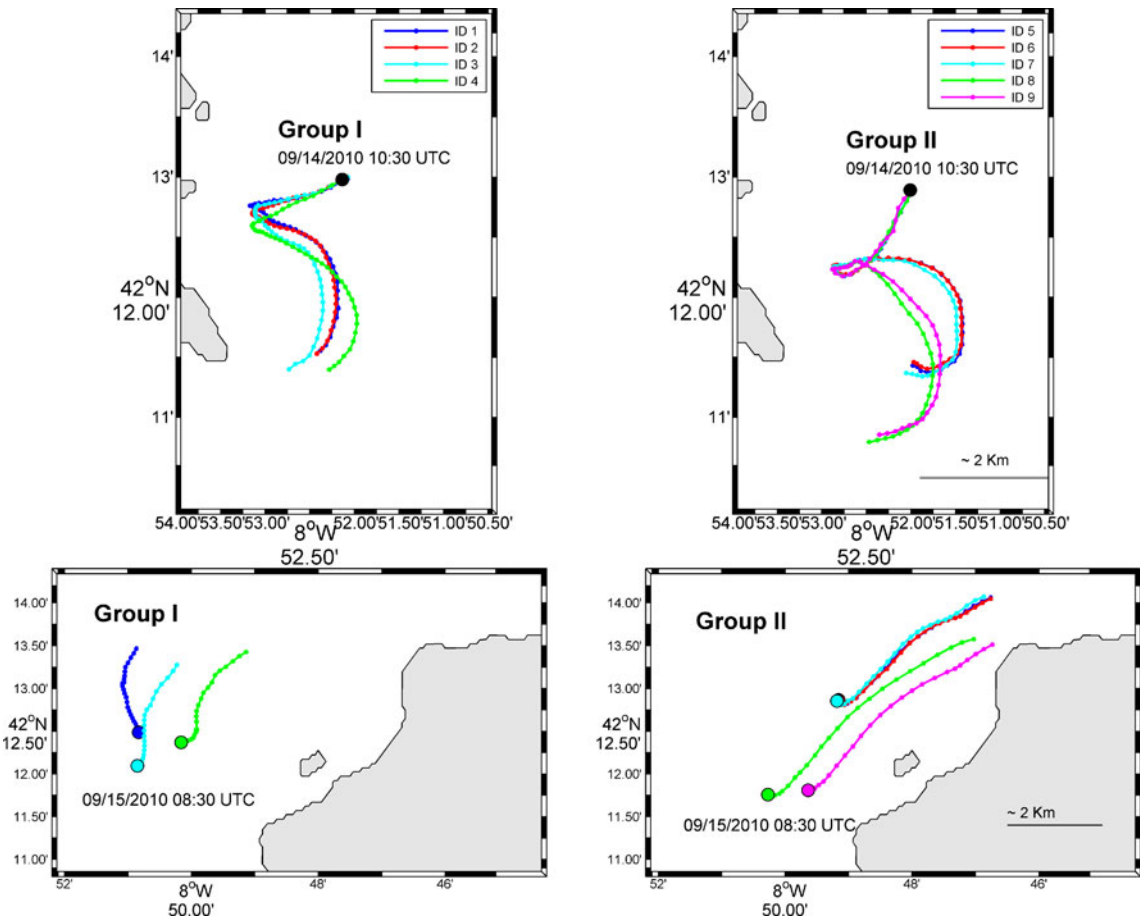

Fig. 5 Buoys trajectories for the first and second period are shown in the *upper* and *lower panel*, respectively. Trajectories of group I and II are presented on the *left* and *right panels*. The initial time of each buoy trajectory is indicated by *solid circles* and the *date*. The final time is indicated in Table 1

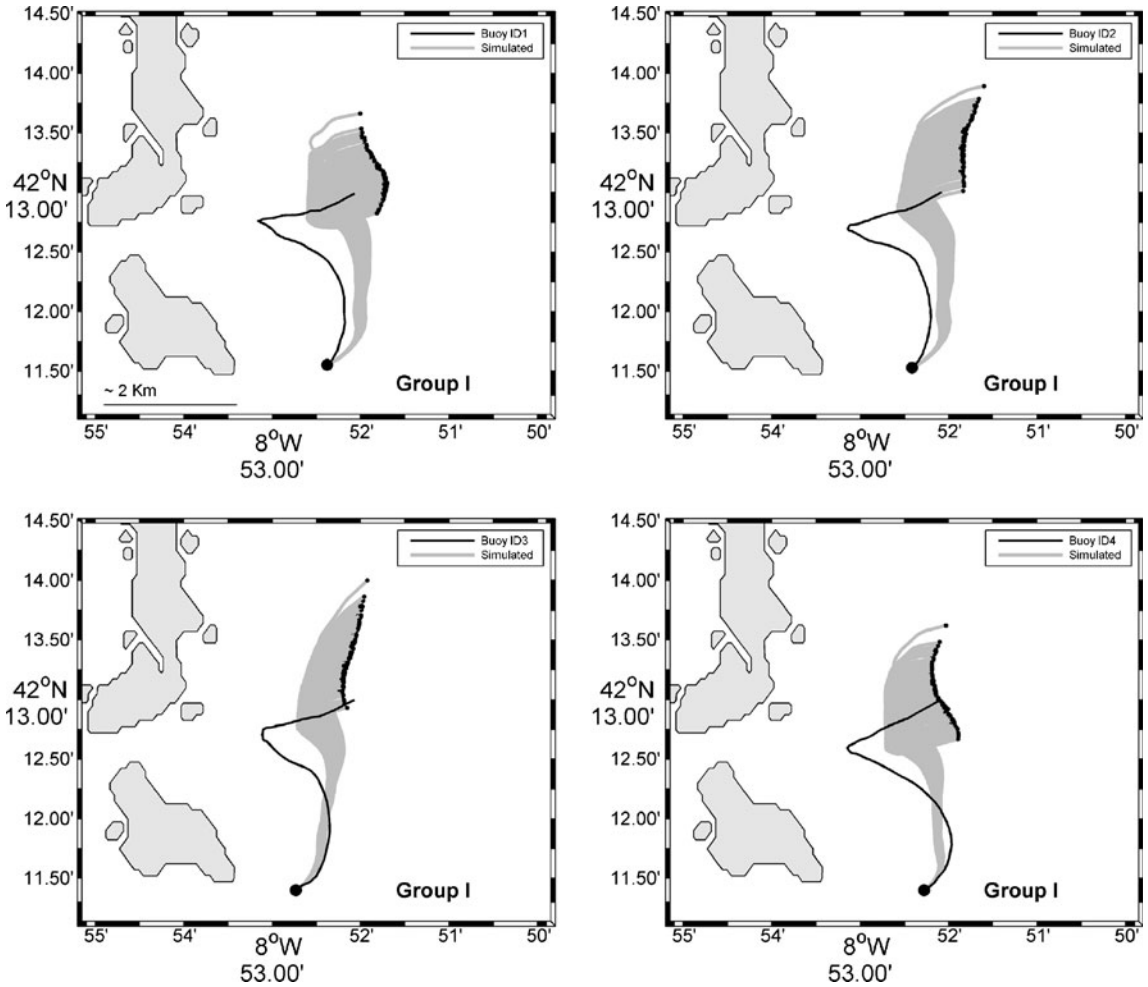

Fig. 6 Observed (*black*) and simulated backward trajectories (*grey*) computed for group I in the first period. The buoy trajectories span from September 14 10:30 UTC to September 14 22:00 UTC. The initial time and position of the simulations are indicated by the *black circles*. The *black dots* stand for the final position of the backtracked trajectories

Figs. 6, 7, 8 and 9 do not contain the actual trajectories. This is one of the main drawbacks of Lagrangian simulations both for forecasting and backtracking, which usually are not able to reproduce the actual trajectories. This uncertainty in Lagrangian simulations highlights the importance of analysing the accuracy of the simulated trajectories and taking it into account for properly defining the search area of a drifting object. As will be shown later, the separation found

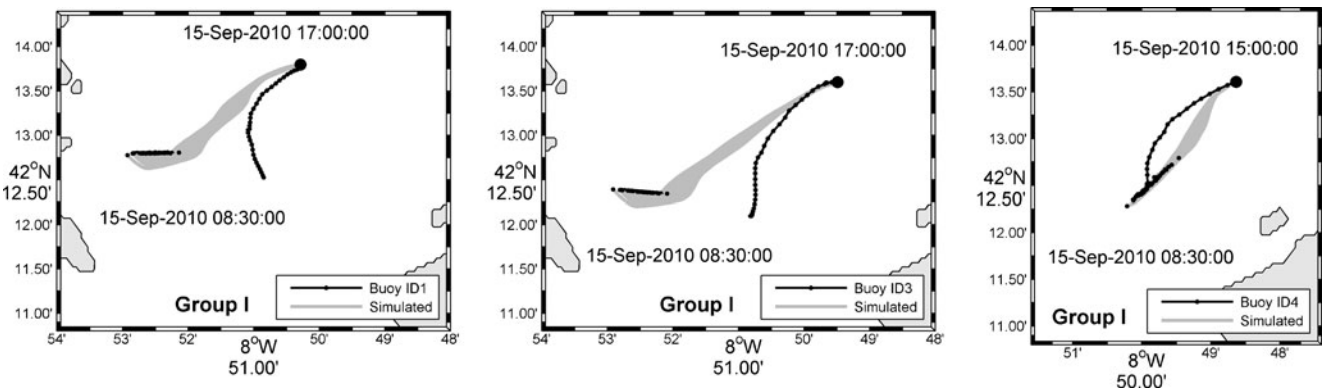

Fig. 7 Observed (*black*) and simulated backward trajectories (*grey*) computed for group I in the 2nd period. The initial time and position of the simulations are indicated by the *black circles*. The *black dots* stand for the final position of the backtracked trajectories. The initial and final date of the buoy trajectories is also shown

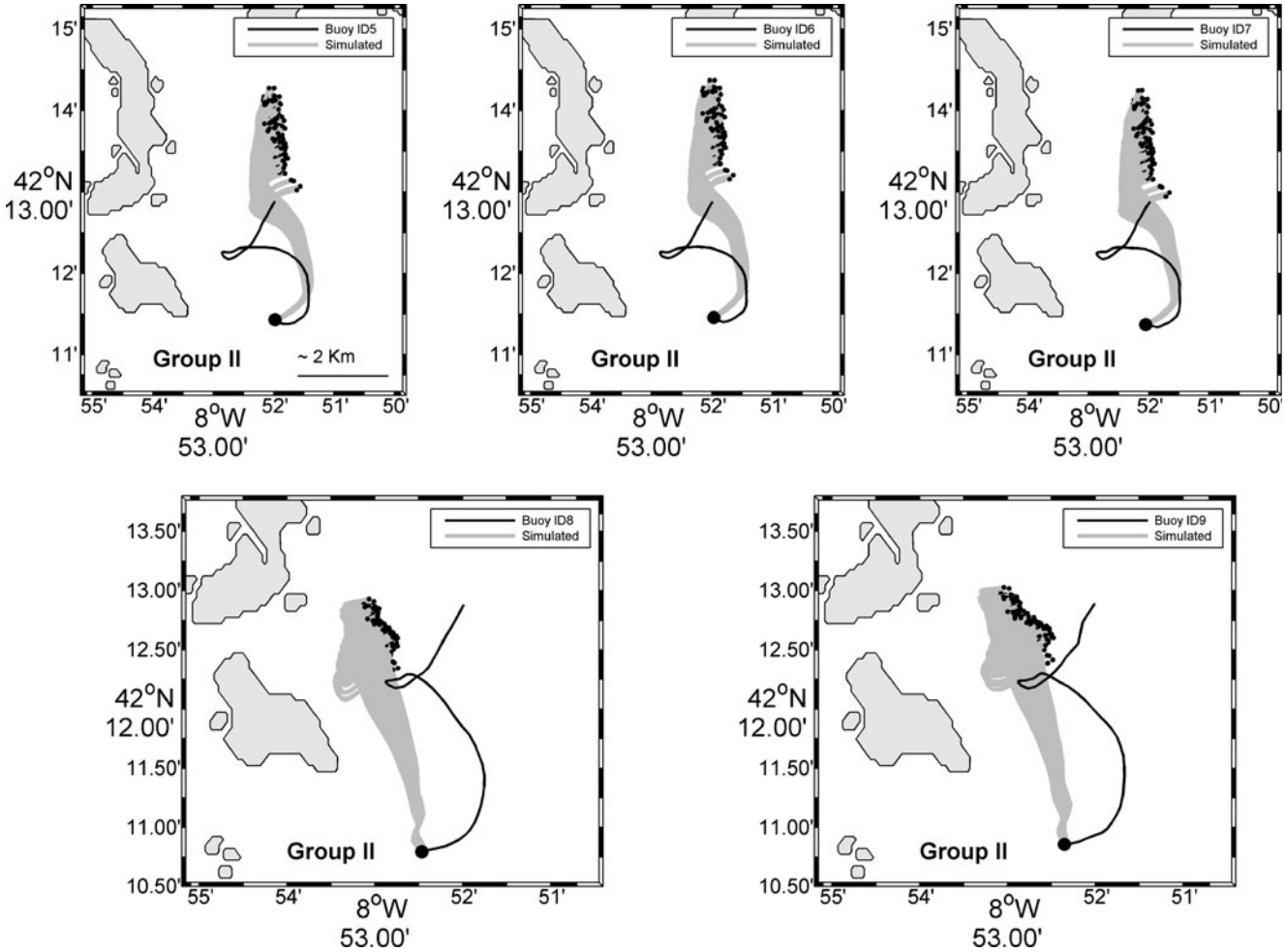

Fig. 8 Observed (*black*) and simulated backward trajectories (*grey*) computed for group II in the first period. The buoy trajectories span from September 14 10:30 UTC to September 14 22:00 UTC. The initial time and position of the simulations are indicated by the *black circles*. The *black dots* stand for the final position of the backtracked trajectories

in this work between actual and simulated backward trajectories for period 1 and period 2 has the same order of magnitude or lower than previous studies reported in the literature (Al-Rabeh et al. 2000; Sebastiao and Soares 2006; Ullman et al. 2006; Sotillo et al. 2008; Rixen et al. 2008; Abascal et al. 2009b), suggesting a good agreement between actual and numerical trajectories.

The accuracy of the simulations was measured by the distance (d) between the actual and the simulated trajectories, defined as the minimum distance between the buoy position and the curve that contains 95 % of the N-simulated positions (95 % confidence area). This distance was computed for every time step of the simulated periods. As previously mentioned, to evaluate the curve that limits the 95 % confidence area, a bivariate kernel estimator (Martinez and Martinez 2002) was applied (see "Section 3.3"). As an illustrative example, Fig. 10 shows the kernel distribution function that corresponds to the final position of the backtracked trajectory for one of the buoys of group I (see upper left panel of Fig. 6). The black dots indicate the final position of the N simulated trajectories and the black line shows the curve which includes 95 % of the simulated data. The comparison between the buoy trajectory and the numerical simulations for the selected period is shown in Fig. 11. The curve that includes 95 % of the numerical positions at the end of the simulation is indicated with a black line. The positions outside of this curve are indicated with black dots. At the end of the simulated period, the separation between the origin of the buoy and the numerical position is about 250 m.

In each group of buoys, the temporal evolution of d was calculated for each buoy and averaged over the total number of buoys, according to the following equation:

$$d_{\mathrm{m}}(t) = \frac{1}{N_B} \sum_{i=1}^{N_{\mathrm{B}}} d(t)_i \tag{8}$$

where d_{m} is the average separation distance, t is the time and N_{B} is the number of buoys for each group.

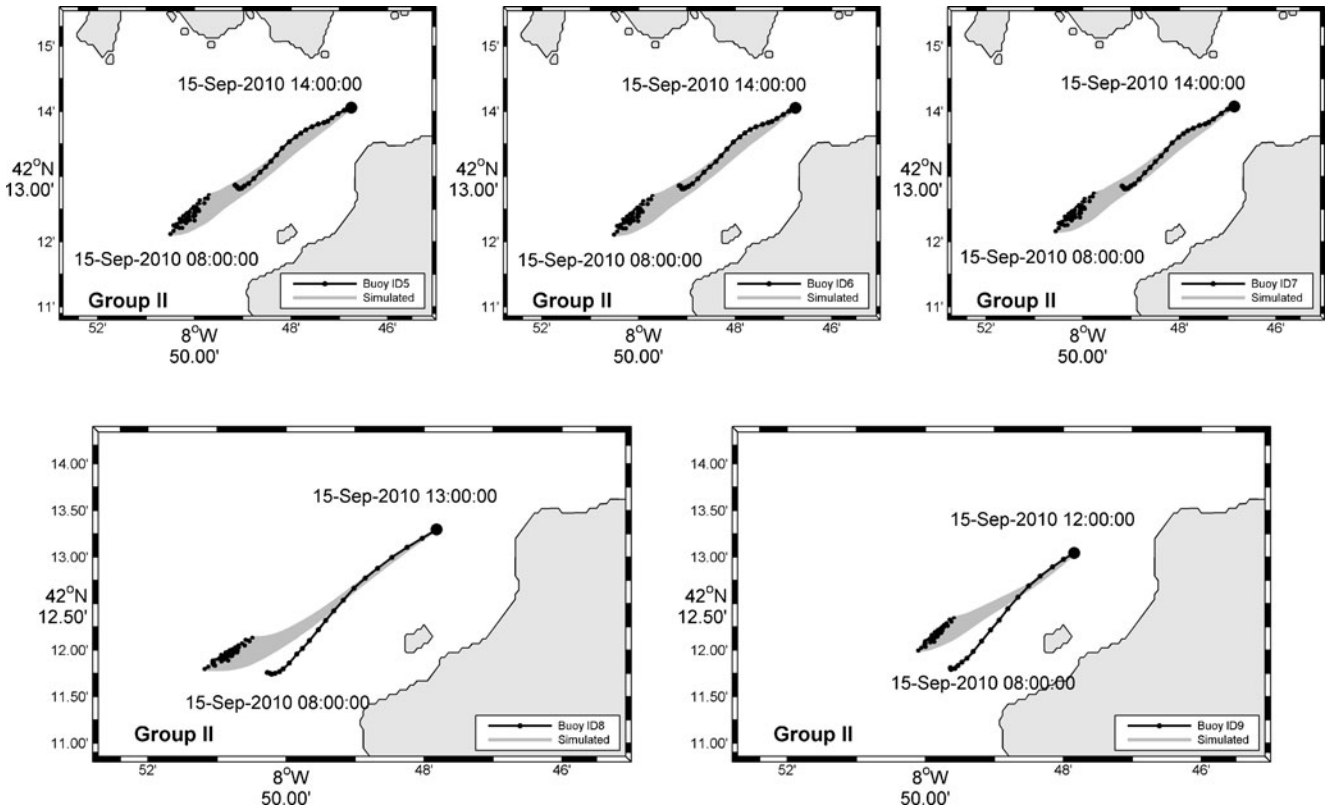

Fig. 9 Observed (*black*) and simulated backward trajectories (*grey*) computed for group I in the second period. The initial time and position of the simulations are indicated by the *black circles*. The *black dots* stand for the final position of the backtracked trajectories. The initial and final date of the buoy trajectories is also shown

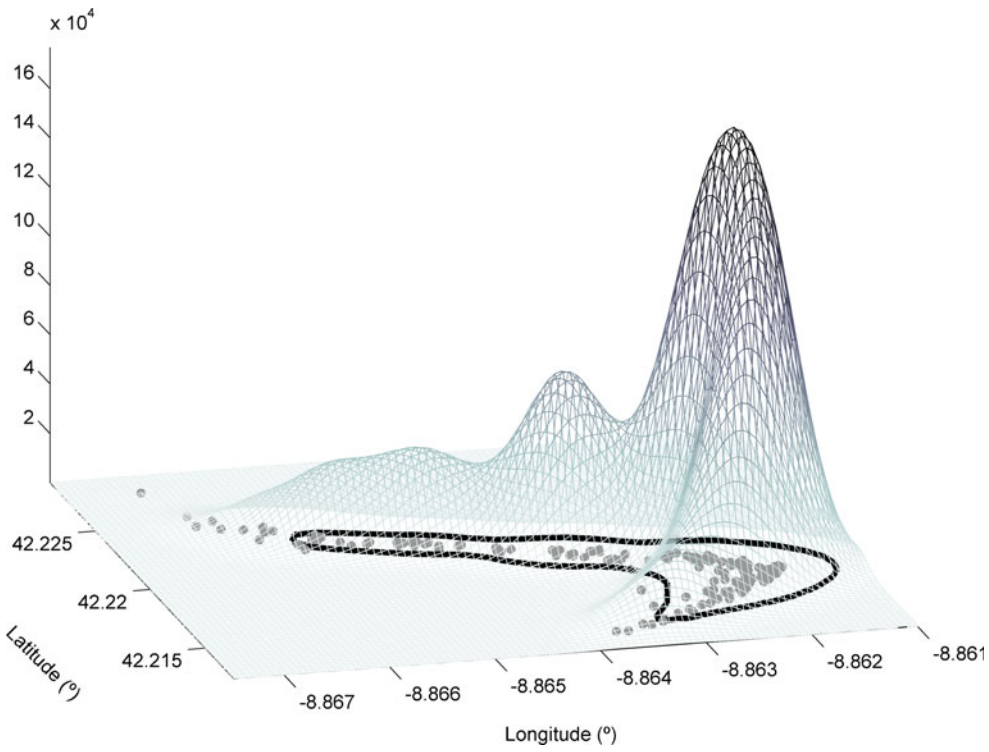

Fig. 10 Kernel density estimates for the final position of the simulated period of buoy number 1 of group I (see upper left panel of Fig. 6). The *grey dots* stand for the numerical positions of the 1,000 simulated backward trajectories. The curve that includes 95 % of the numerical data is represented by the *black line*

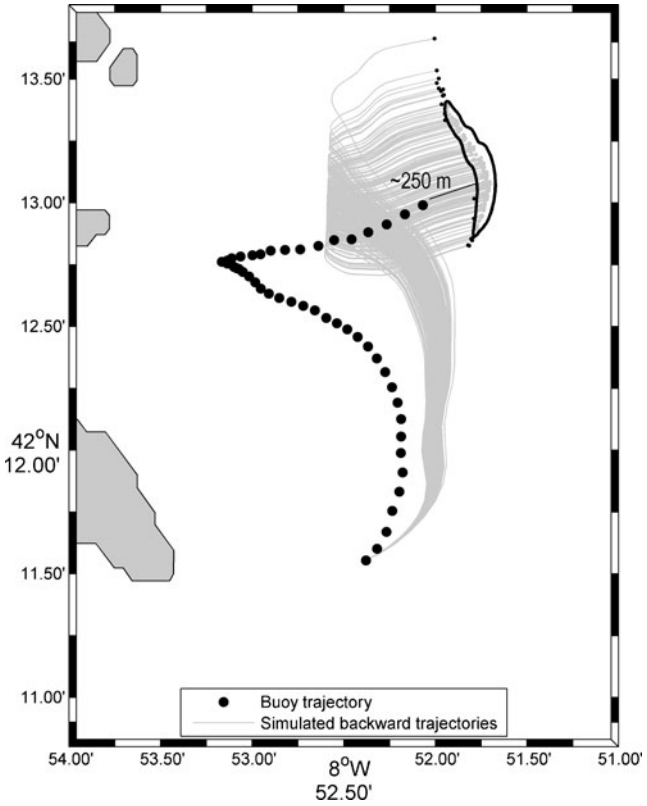

Fig. 11 Comparison between the buoy path and the backtracked trajectory of buoy number 1 of group I (see upper left panel of Fig. 6). The curve that includes 95 % of the final numerical positions is represented by the *black line*. The final separation (d) between the buoy location and the numerical results is about 250 m

Figures 12 and 13 show the temporal evolution of d_m (black line) and the standard deviation (grey line) for the first and second period. Results obtained for group I show that the separation distance is mostly less than or equal to 1 km over each simulated period (see Figs. 12a and 13a). The mean value of d_m is 0.41 and 0.72 km for period 1 and 2, respectively. The maximum error of the simulations ranges between 0.77 km (period 1) and 1.74 km (period 2). Note that the errors increase significantly at the end of period 2 (see Fig. 13a). This result is in agreement with the backtracked trajectories shown in Fig. 7, which shows that the numerical backtracked trajectory for buoys 1 and 3 deviates from the actual trajectories at the end of the simulation. These discrepancies could be related with inaccuracies in the forcing fields, which are highly affecting the accuracy of the simulations performed.

For group II, the separation distance is less than 1.5 km over each simulated period (see Figs. 12b and 13b). The mean value of d_m is 0.84 and 0.62 km for period 1 and 2, respectively, showing a good agreement between numerical and actual trajectories. In this case, the maximum error obtained for the simulations performed is 1.4 km (period 1) and 1.15 km (period 2). It is important to highlight that the accuracy of the simulations for the second period is of the same order of magnitude as that of the first one. These results show that the coefficients obtained in the first period are appropriate to backtrack the trajectories of the second one.

Regarding the comparison between the different behaviours of both groups of buoys, most backtracked trajectories for group I in period 1 show lower errors than the simulations for group II. This result is consistent with the paths followed by the buoys. At the end of the fist period (14/09/2010 22:00 UTC), buoys belonging to group I remained closer than buoys of group II (see Fig. 5). Note that buoy numbers 8 and 9 in group II (see Fig. 5) drifted southward faster than the rest of the buoys. This variability shows the complexity of the problem and the difficulty in calculating the origin of a drifting object following an observation.

In order to take into account this natural variability, the error in the numerical simulations was compared with the dispersion of the buoys. To achieve this objective, the root mean square error (RMSE) of the actual drifters from their mean cluster position was determined (see Fig. 14) and compared with the final separation between the actual and the simulated backward trajectories (see Table 3). It is worth mentioning that the uncertainty in the estimation of the origin of the actual trajectories for the first period was of the same

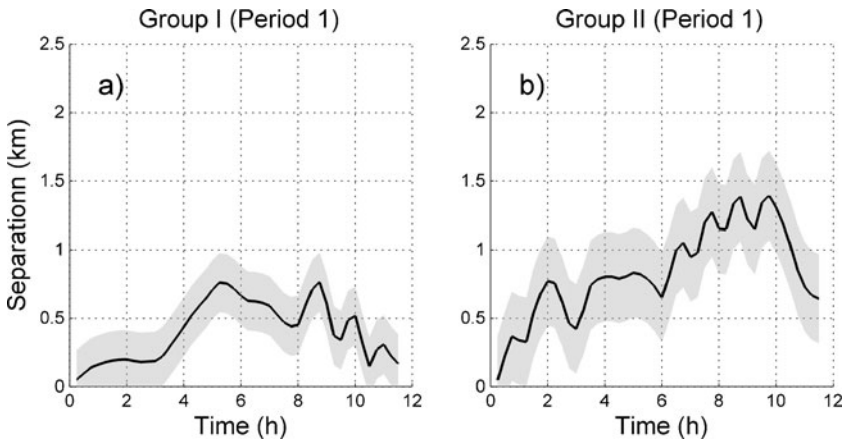

Fig. 12 Distance between the actual and simulated backward trajectories as a function of time (averaged over all simulated buoy trajectories) for period 1. **a** Results for group I and **b** for group II. The mean value and the standard deviation are represented by the *black line* and the *grey area*, respectively. The *x*-axis represents time (hours) from the starting point of the simulation

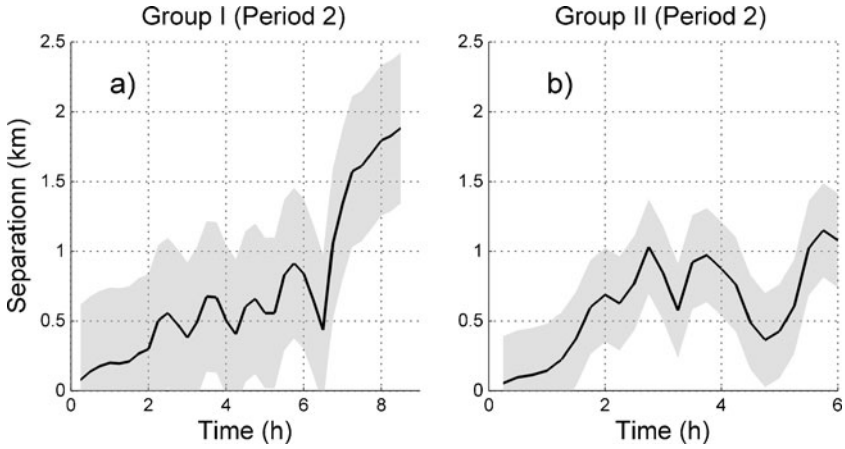

Fig. 13 Distance between the actual and simulated backward trajectories as a function of time (averaged over all simulated buoy trajectories) for period 2. **a** Results for group I and **b** for group II. The mean value and the standard deviation are represented by the *black line* and the *grey area*, respectively. The *x*-axis represents time (hours) from the starting point of the simulation

order of magnitude as the dispersion of the buoy trajectories (see Fig. 14 and Table 3). However, the uncertainty increases in the second period and is highly affected by the discrepancies observed in buoy numbers 1 and 3 (see Fig. 7).

For groups I and II, the error in the estimation of the origin of the buoy trajectories was calculated by means of the RMSE of the separation between actual and simulated backtrack trajectories at the end of each simulated period (Table 3) according to the following equation:

$$R_{\mathrm{G}} = \sqrt{\frac{\sum_{i}^{N} d_{\mathrm{end}}^2}{N_{\mathrm{S}}}} \tag{9}$$

where R_{G} is the RMSE for each group, d_{end} is the final separation between the actual and simulated trajectories and N_{S} is the number of simulated trajectories. Taking into account the values shown in Table 3, R_{G} was found to be 1.01±0.85 km for group I and 0.82±0.26 km for group II. Note that the value of RMSE for group I is highly influenced by the discrepancies observed for buoys 1 and 3 during the second period (see Fig. 7).

For practical reasons, the squared difference between the simulation and actual buoy position provides a better error index than the simple linear distance. This is due to the fact that the search and rescue operations are based within the area of exploration. To take this into account, the search area was calculated in terms of circles of RMSE radius (see Eq. (9)), obtaining 3.2 and 2.11 km^2 for groups I and II, respectively. These circles represent the mean optimal search area to be scanned to find the origin of the drifting buoys. Figures 15 and 16 show examples of search areas to find the origin of buoy number 1 (group I) and number 9 (group II) for the first and second period, respectively.

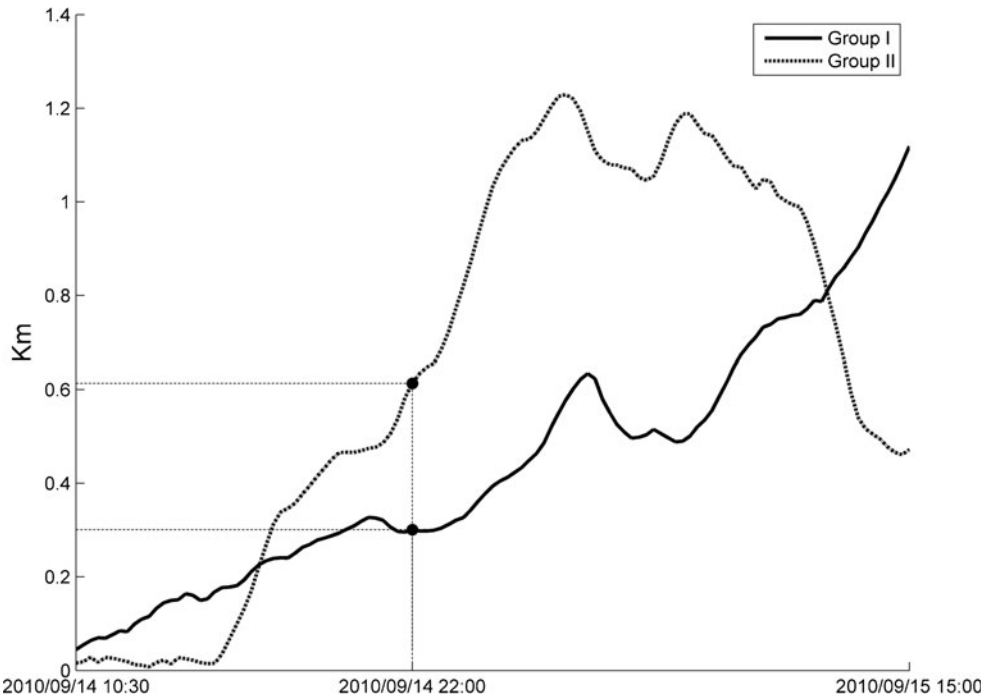

Fig. 14 RMSE of the actual drifters from their mean cluster position

Table 3 Final separation (km) between the actual and the simulated backward trajectory for each computed buoy trajectory. Note that, for period 2, the simulated trajectories have different lengths (see Table 1)

Group	Buoy (ID)	Final separation (km)	
		Period 1	Period 2
I	1	0.26	1.87
	2	0.17	
	3	0.17	1.88
	4	0.06	0.06
II	5	0.71	1.07
	6	0.96	1.15
	7	0.58	1.02
	8	0.63	0.72
	9	0.34	0.63

5 Conclusions

In this paper, the contribution of the HF radar technology for backtracking drifting objects was studied using a Lagrangian trajectory model. High-resolution currents measured by coastal HF radar systems combined with atmospheric fields provided by numerical models were used to backtrack the trajectory of two dataset of drifting buoys: (1) buoys with 60 cm drogue (group I) and (2) buoys without drogue (group II). For each dataset of buoys, the transport model was calibrated using the SCEM-UA algorithm in order to obtain the optimal value of the coefficients and to analyse their level of significance in the transport model. Results of the calibration show that for both groups the optimal mean $\widehat{C}_{\mathrm{D}}$ value is smaller than the most common value (3 % of the wind speed). For group I, $\widehat{C}_{\mathrm{D}}$ was found to be close to 0, suggesting that the contribution of atmospheric fields to simulate the buoy trajectories could be discarded for calm wind conditions. Regarding group II, with 95 % confidence level, the optimal mean value was found to be $\widehat{C}_{\mathrm{D}} = 0.015$. As stated before, this value is smaller than the typical 3 % wind speed used in the literature (ASCE 1996), suggesting that $\widehat{C}_{\mathrm{D}}$ accounts for the direct wind stress (sailing effect) whereas the HF radar currents contain the wind-induced component of the ocean surface current. The high $\widehat{C}_{\mathrm{C}}$ values obtained for both groups suggest a quite good agreement between the real current field and the radar HF current measurements. These results represent an improvement with respect to a similar analysis performed using numerical currents data (Abascal et al. 2009a) and currents provided by long-range HF radar systems (Abascal et al. 2009b).

A comparison of the results obtained for groups I and II shows that wind forcing presents a higher relevance in the motion of the buoys belonging to group II, whereas it could be practically discarded for simulating the trajectories of group I. Taking into account that the average effective depth of short-range HF (operating in the vicinity of 46 Mhz) radar is 0.25 m, a strong influence of HF radar currents in the transport of this kind of buoys could be expected. These results suggest that, under calm wind conditions, HF radar currents could be used as a unique forcing to simulate the trajectory of surface drifting buoys with a small drogue (~60 cm). Moreover, these results also suggest that, to simulate the trajectory of surface drifting buoys without drogue, both currents and wind fields are required. However, further study is required to study the influence of different ocean–meteorological conditions on the drifting trajectory and to analyse how these environmental conditions affect the contribution of HF radar currents in the transport of the buoys. Besides the influence of buoy features on the drifting trajectory, these results show the importance of properly determining the relative contribution of each forcing in the transport and the appropriate coefficients in order to optimize the model results.

Once calibrated, the model was used to backtrack the trajectory of the buoys for two different periods: (1) the first one corresponding to the period used for the calibration of the

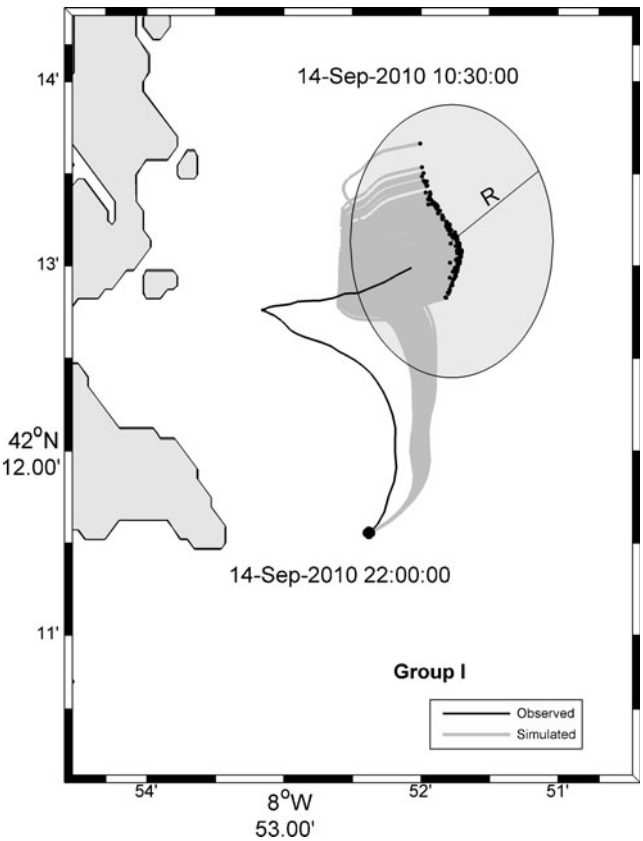

Fig. 15 Search area (*grey circle*) to find the origin of buoy number 1 (group I) in the first period (R=1.01 km). Actual and simulated backward trajectories are indicated by *black* and *grey lines*. The buoy trajectory spans from September 14 10:30 UTC to September 14 22:00 UTC. The initial time and position of the simulation is indicated by the black circle. The *black dots* stand for the final position of the backtracked trajectories

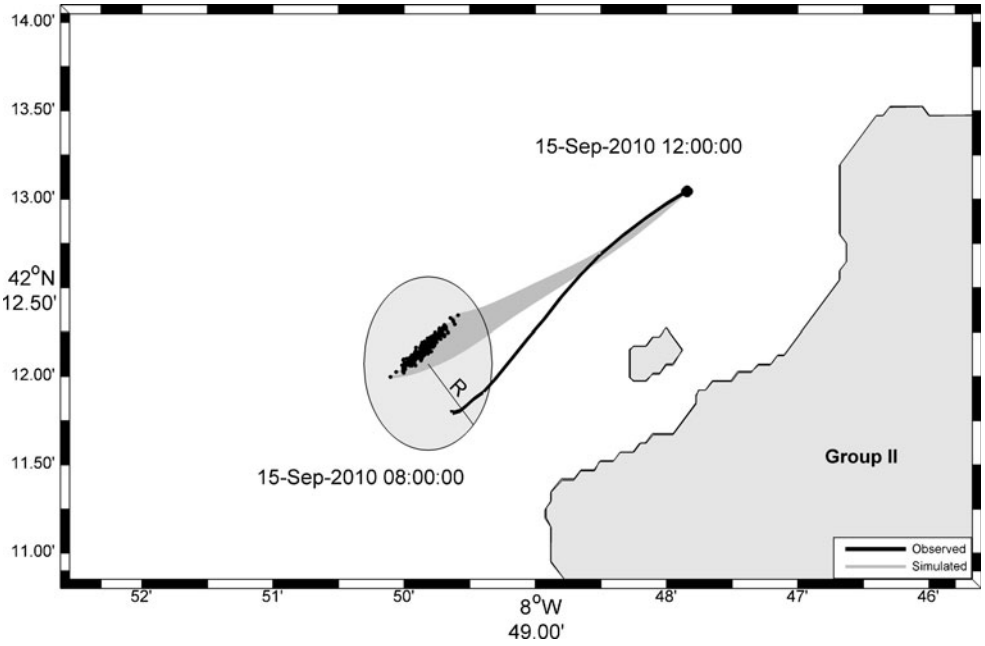

Fig. 16 Search area (*grey circle*) to find the origin of buoy number 9 (group II) in the second period (R=0.82 km). Actual and simulated backward trajectories are indicated by *black* and *grey lines*. The buoy trajectory spans from September 15 08:00 UTC to September 15 22:00 UTC. The initial time and position of the simulation is indicated by the *black circle*. The *black dots* stand for the final position of the backtracked trajectories

model and (2) the second one corresponding to the period after the HF radar data gap, which represents an independent dataset. The buoy trajectories were computed by means of Monte Carlo simulation using the N optimal combination of model parameters obtained in the calibration process.

The accuracy of the simulations performed was measured by the distance between the actual and the simulated backward trajectories. For group I, the temporal evolution of d_m presents a mean value of 0.41 km for period 1 and 0.72 km for period 2. Regarding group II, this value increases to 0.84 km for period 1 and decreases to 0.62 km for period 2. Similar accuracy was found for both periods, suggesting that the coefficients obtained in the first period are appropriate to backtrack the trajectories in the second one.

The RMSE of the simulated origin compared with the real position was 1.01±0.85 km for group I and 0.82± 0.26 km for group II. Based on these results, a search area was calculated in terms of circles of RMSE radius, obtaining 3.2 and 2.11 km^2 for groups I and II, respectively. These results represent the mean optimal search area to be scanned to find the origin of the drifting buoys.

This study has demonstrated that measured data provided by HF radar, combined with modelled winds, are of value for backtracking of floating objects. It is important to highlight the short period and calm conditions of the available dataset for this study. Further studies are required using a large dataset of buoys that represent the ocean and meteorological characteristics of the study area. The larger the database, the greater the representativeness of the coefficients for the study area.

Moreover, longer and more continuous buoys and HF radar data are required to study the accuracy of the simulations using a longer simulation horizon. Note that, although a larger database would be desirable, for SAR operations the first hours could be crucial. Thus, to study the trajectory evolution in a short period of time can be critical when, for example, a person is in the water and there is a risk of hypothermia.

Although the validation has been performed using drifting buoys, the results could be also applied for other floating objects or floating substances such as oil slicks. Further studies are required to analyse the differences between different floating objects and to establish the drift properties of different objects (Allen and Plourde 1999; Breivik et al. 2011).

Acknowledgments This work has been partially funded by the Spanish Ministry for Science and Innovation under the research projects PSE-310000-2009-03 (PSE PROMARES, OCTOPOS subproject) and TRA2011-28900 (PLVMA project). The authors would like to thank the Galician Coast Guard, INTECMAR, the University of Vigo, Puertos del Estado and MeteoGalicia for the collaboration and the data provided for the study.

References

Abascal AJ, Castanedo S, Gutierrez AD, Comerma E, Medina R, Losada IJ (2007) TESEO, an operational system for simulating oil spills trajectories and fate processes. Proceedings ISOPE-2007: The 17th International Offshore Ocean and Polar Engineering Conference. Lisbon, Portugal, The International Society of Offshore Ocean and Polar Engineers (ISOPE) 3:1751–1758

Abascal AJ, Castanedo S, Mendez FJ, Medina R, Losada IJ (2009a) Calibration of a Lagrangian transport model using drifting buoys deployed during the *Prestige* oil spill. J Coast Res 25(1):80–90

Abascal AJ, Castanedo S, Medina R, Losada IJ, Alvarez-Fanjul E (2009b) Application of HF radar currents to oil spill modelling. Mar Pollut Bull 58:238–248

Allen AA, Plourde JV (1999) Review of Leeway; field experiments and implementation. USCG & R&D Center Technical Report CG-D-08-99

Allen-Perkins S, Montero P, Ayensa G (2010) Testing and application of buoys to follow up spills. Drifter workshop, Vigo (Spain)

Al-Rabeh AH, Lardner RW, Gunay N (2000) Gulfspill Version 2.0: a software package for oil spills in the Arabian Gulf. Environ Model Softw 15:425–442

Ambjörn C (2008) Seatrack Web forecasts and backtracking of oil spills—an efficient tool to find illegal spills using AIS. US/EU-Baltic International Symposium, IEEE/OES

ASCE (1996) State-of-the-art review of modeling transport and fate of oil spills. ASCE Committee on Modeling Oil Spills. Water Resources Engineering Division. J Hydraul Eng 122(11):594–609

Balseiro CF (2008) MeteoGalicia final report. Easy Project

Barrick DE, Evens MW, Weber BL (1977) Ocean surface currents mapped by radar. Science 198:138–144

Beegle-Krause CJ (2001) General NOAA Oil Modeling Environment (GNOME): a new spill trajectory model. International Oil Spill Conference

Breivik Ø, Allen AA (2008) An operational search and rescue model for the Norwegian Sea and the North Sea. J Mar Syst 69(1–2):99–113

Breivik Ø, Allen AA, Maisondieu C, Roth JC (2011) Wind-induced drift of objects at sea: the leeway field method. Appl Ocean Res 33(2):100–109

Castanedo S, Medina R, Losada IJ, Vidal C, Méndez FJ, Osorio A, Juanes JA, Puente A (2006) The *Prestige* oil spill in Cantabria (Bay of Biscay). Part I: operational forecasting system for quick response, risk assessment and protection of natural resources. J Coast Res 22(6):1474–1489

Chapman RD, Graber HC (1997) Validation of HF radar measurements. Oceanography 10:76–79

Chapman RD, Shay LK, Graber HC, Edson JB, Karachintsev A, Trump CL, Ross DB (1997) On the accuracy of HF radar surface current measurements: intercomparisons with ship-based sensors. J Geophys Res 102(8):18737–18748

Christiansen BM (2003) 3D oil drift and fate forecast at DMI. Technical report no. 03-36. Danish Meteorological Institute, Denmark

Daniel P, Marty F, Josse P, Skandrani C, Benshila R (2003) Improvement of drift calculation in MOTHY operational oil spill prediction system. Proceedings of the 2003 International Oil Spill Conference. Washington, DC: American Petroleum Institute

Davidson FJM, Allen A, Brassington GB, Breivik Ø, Daniel P, Kamachi M, Sato S, King B, Lefevre F, Sutton M, Kaneko H (2009) Applications of GODAE ocean current forecasts to search and rescue and ship routing. Oceanography 22(3):176–181

Duan Q, Sorooshian S, Gupta V (1992) Effective and efficient global optimization for conceptual rainfall–runoff models. Water Resour Res 28(4):1015–1031

Edwards KP, Werner FE, Blanton BO (2006) Comparison of observed and modeled drifter trajectories in coastal regions: an improvement through adjustments for observed drifter slip and errors in wind fields. J Atmos Ocean Technol 23(11):1614–1620

Fernández V, Ferrer MI, Abascal AJ, Castanedo S, Medina R, Alvarez E (2010) Operational applications of coastal high-frequency (HF) radar technology for oil spill operations. I Encuentro Oceanografía Física Española, Barcelona (Spain)

Griffa A, Piterbarg LI, Ozgokmen T (2004) Predictability of Lagrangian particle trajectories: effects of smoothing of the underlying Eulerian flow. J Mar Res 62:1–35

Hackett B, Breivik Ø, Wettre C (2006) Forecasting the drift of objects and substances in the oceans. In: Chassignet EP, Verron J (eds) Ocean weather forecasting: an integrated view of oceanography. Springer, Dordrecht, pp 507–524

Hodgins DO (1991) New capabilities in real-time oil spill and fate prediction using HF radar remote sensing. Proceedings of the 14th AMOP Technical Seminar, Canada

Hunter JR, Craig PD, Phillips HE (1993) On the use of random walk models with spatially variable diffusivity. J Comp Phys 106:366–376

Kohut JT, Roarty HJ, Glenn SM (2006) Characterizing observed environmental variability with HF Doppler radar surface current mappers and acoustic Doppler current profilers: environmental variability in the coastal ocean. J Ocean Eng 31(4):876–884

Lipa BJ, Barrick DE (1983) Least-squares methods for the extraction of surface currents for CODAR cross/loop data application at ARSLOE. IEEE J Ocean Eng OE-8:226–253

Maier-Reimer E (1982) On tracer methods in computational hydrodynamics. In: Abbott MB, Cunge JA (eds) Engineering application of computational hydraulics, 1 (Chapter 9). Pitman, London

Martinez WL, Martinez AR (2002) Computational statistics handbook (Chapter 8). Chapman and Hall, Boca Raton

Miranda R, Braunschweig F, Leitão P, Neves R, Martins F, Santos A (2000) MOHID 2000, a coastal integrated object oriented model. Hydraulic Engineering Software VII. WIT, Southampton

O'Donnell J, Ullman D, Spaulding M, Howlett E, Fake T, Hall P, Tatsu I, Edwards C, Anderson E, McClay T, Kohut J, Allen A, Lester S, Lewandowski M (2005) Integration of Coastal Ocean Dynamics Application Radar (CODAR) and Short-Term Prediction System (STPS) surface current estimates into the Search and Rescue Optimal Planning System (SAROPS). US Coast Guard Tech. Rep., DTCG39-00-D-R00008/HSCG32-04-J-100052

Price JM, Reed M, Howard MK, Johnson WR, Zhen-Gang J, Marshall CF, Guinasso JRNL, Rainey GB (2006) Preliminary assessment of an oil-spill trajectory model using a satellite-tracked, oil-spill-simulating drifters. Environ Model Softw 21:258–270

Reed M, Turner C, Odulo A (1994) The role of wind and emulsification in modelling oil spill and surface drifter trajectories. Spill Sci Technol Bull 1(2):143–157

Rixen M, Ferreira-Coelho E, Signell R (2008) Surface drift prediction in the Adriatic Sea using hyper-ensemble statistics on atmospheric, ocean and wave models: uncertainties and probability distribution areas. J Mar Syst 69(1–2):86–98

Sebastiao P, Soares CG (2006) Uncertainty in predictions of oil spill trajectories in a coastal zone. J Mar Syst 63:257–269

Skamarock WC, Klemp JB, Dudhia J, Gill DO, Barker DM, Wang W, Powers JG (2005) A description of the Advanced Research WRF version 2. NCAR technical note NCAR/TN-468+STR, 88 pp

Sotillo MG, Alvarez Fanjul E, Castanedo S, Abascal AJ, Menendez J, Olivella R, García-Ladona E, Ruiz-Villareal M, Conde J, Gómez M, Conde P, Gutierrez AD, Medina R (2008) Towards an operational system for oil spill forecast in the Spanish waters: initial developments and implementation test. Mar Pollut Bull 56 (4):686–703

Spaulding ML, Howlett E, Anderson E, Jayko K (1992) OILMAP: a global approach to spill modelling. 15th Annual Arctic and marine Oilspill Program, Technical Seminar, Edmonton

Stewart RH, Joy JW (1974) HF radio measurements of surface currents. Deep-Sea Res 21:1039–1049

Ullman D, O'Donnell J, Edwards C, Fake T, Morschauser D, Sprague M, Allen A, Krenzien B (2003) Use of Coastal Ocean Dynamics Application Radar (CODAR) technology in U. S. Coast Guard search and rescue planning. US Coast Guard Rep., CG-D-09-03. 40 pp

Ullman DS, O'Donnell J, Kohut J, Fake T, Allen A (2006) Trajectory prediction using HF radar surface currents: Monte Carlo simulations of prediction uncertainties. J Geophys Res 111(C12005):1–14

Varela R (2010) Implementación de un sistema radar de alta frecuencia en la Ria de Vigo. Características fundamentales. I Encuentro Oceanografía Física Española, Barcelona (España)

Vrugt JA, Gupta HV, Bouten W, Sorooshian S (2003a) A Shuffled Complex Evolution Metropolis algorithm for optimization and uncertainty assessment of hydrologic model parameters. Water Resour Res 39(8) 1201:1–8 1–16

Vrugt JA, Gupta HV, Bouten W, Sorooshian S (2003b) Shuffled Complex Evolution Metropolis (SCEM-UA) algorithm. Manual, version 1.0. 24 pp